Controlled grain-size thermochromic VO_2 coatings by the fast oxidation of sputtered vanadium or vanadium oxide films deposited at glancing angles

A.J. Santos , B. Lacroix , M. Domínguez , R. García , N. Martin , F.M. Morales

PII: S2468-0230(21)00653-2
DOI: https://doi.org/10.1016/j.surfin.2021.101581
Reference: SURFIN 101581

To appear in: *Surfaces and Interfaces*

Received date: 10 August 2021
Revised date: 14 October 2021
Accepted date: 31 October 2021

Please cite this article as: A.J. Santos , B. Lacroix , M. Domínguez , R. García , N. Martin , F.M. Morales , Controlled grain-size thermochromic VO_2 coatings by the fast oxidation of sputtered vanadium or vanadium oxide films deposited at glancing angles, *Surfaces and Interfaces* (2021), doi: https://doi.org/10.1016/j.surfin.2021.101581

Controlled grain-size thermochromic VO_2 coatings by the fast oxidation of sputtered vanadium or vanadium oxide films deposited at glancing angles

A. J. Santos[a,b,*] mailto:antonio.santos@uca.es, B. Lacroix[a,b], M. Domínguez[a,c], R. García[a,b], N. Martin[d] and F. M. Morales[a,b]

[a]IMEYMAT: Institute of Research on Electron Microscopy and Materials of the University of Cádiz, Spain

[b]Department of Materials Science and Metallurgic Engineering, and Inorganic Chemistry, Faculty of Sciences, University of Cádiz, Spain

[c]Department of Condensed Matter Physics, Faculty of Sciences, University of Cádiz, 11510 Puerto Real, Cádiz, Spain

[d]Institut FEMTO-ST, UMR 6174 CNRS, Université Bourgogne Franche-Comté, 15B, Avenue des montboucons 25030 Besançon Cedex, France

[*]Corresponding author.

Graphical Abstract

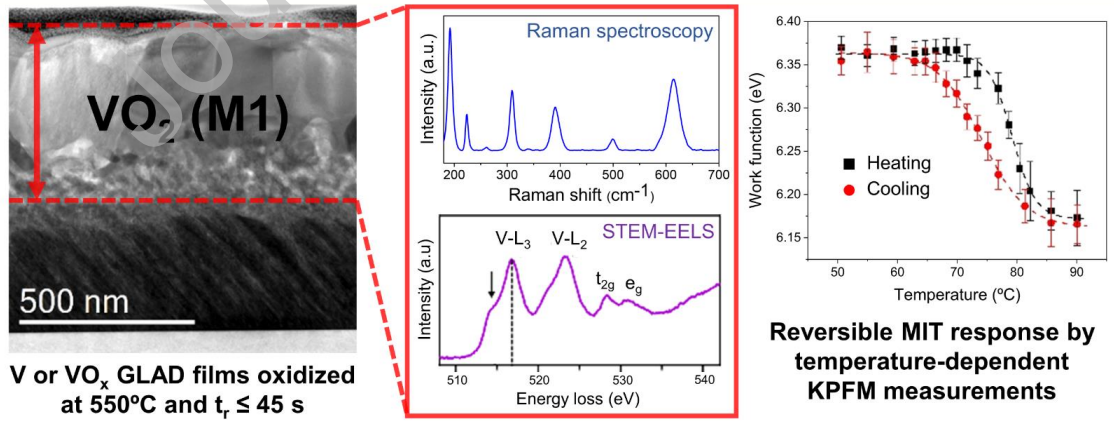

Highlights

- Deposition of V or VO_x GLAD films by combining GLAD and RGPP approaches.
- Fast post-deposition oxidation of such systems in air to attain thermochromic VO_2.
- High control of VO_2 grain size and crystallinity by adjusting reaction times.
- Comprehensive characterization by SEM, Raman spectroscopy and (S)TEM methods.
- Evaluation of the MIT response by means of temperature dependant KPFM measurements.

Abstract

An original, simple and cost-effective oxidation strategy to attain thermochromic vanadium dioxide thin films is reported. This two-step procedure comprises the initial deposition of DC magnetron-sputtered vanadium or vanadium oxide films by the combination of glancing angle deposition and, if needed, reactive gas pulsing process, followed by fast oxidation of such layers in air atmosphere at high temperatures. Thanks to the careful control of the thermal treatment parameters, and taking advantage of the superior reactivity of the high surface-to-volume porous deposited structures, the formation of pure VO_2 (M1) layers was achieved. The comprehensive characterization of such oxidized systems by means of scanning electron microscopy, Raman spectroscopy and scanning-transmission electron microscopy techniques such as electron energy-loss spectroscopy, not only confirmed the presence of the VO_2 (M1) phase, but also allowed to shed light on the key role that reaction time plays in the selective formation of vanadium dioxide films of adjustable grain size and crystallinity. The optimal conditions to stabilize thermochromic VO_2 consists in using large deposition angles (85º) and short oxygen pulses (≤ 2 s) during the growth, followed by fast and short thermal treatments (≤ 45 s with a heating rate of 42ºC s^{-1}) in air

atmosphere at 550ºC. The metal-to-insulator response of the accomplished VO_2 layers was finally evaluated by means of temperature dependent Kelvin probe force microscopy measurements, evidencing surface potential drops at heating, greater than those reported in the literature to date for VO_2 thin films.

Keywords: VO_2 thin film, glancing angle deposition, fast oxidation, metal-insulator transition, transmission electron microscopy, EELS spectroscopy, Raman spectroscopy, KPFM.

Introduction

Vanadium oxides (VO_x) have become one of the most extensively studied materials for many years due to their unique properties and technological applications. In this framework, vanadium (IV) oxide (VO_2) has specially attracted the attention of the scientific community since it exhibits a reversible metal-to-insulator phase transition (MIT) between insulating monoclinic VO_2 (M1) to metallic rutile VO_2 (R) during heating at a temperature of ~68 ºC, which implies drastic changes in the optical and electrical properties [1–7]. This makes VO_2 an attractive thermochromic material for applications in smart windows [8–11], resistive switching elements [12,13], storage devices [14] and sensors [15].

Nevertheless, the fabrication of VO_2-based films has become a real challenging issue not only due to the complexity of the vanadium-oxygen reactive system but also because of the narrow stability range of VO_2, which can lead to the formation other more thermodynamically stable oxides such as V_2O_3 and V_2O_5, mixtures of various

stoichiometries, or even the appearance of several VO_2 metastable crystalline polymorphs [2–4,16–18]. Hence, it is clear that the preparation of VO_2 films requires a precise control of the deposition parameters.

Many different approaches, such as sol–gel [19], pulsed laser deposition [20,21], chemical vapor deposition [22], and polymer-assisted deposition [23], have succeeded in synthesizing VO_x films with high VO_2 yields, although the complexity and high cost involved in all these methods become a critical limitation for practical applications. In this context, reactive direct current (DC) magnetron sputtering postulates as one of the most promising and simplest techniques for depositing large-areas of vanadium or vanadium oxide films at low temperature [24–29], so that by adjusting oxygen injection times during the sputtering process, the proportions of V to O on the films can be controlled. As can be found in the literature [15,24,26–28,30–32], many different post-deposition annealing strategies, which are required to obtain VO_2 films with desired compositions and morphologies, have been extensively implemented on magnetron sputtered V or VO_x films. Several of these post-annealing treatments sometimes lack of precise control of key oxidation parameters like reaction temperatures and times or heating and cooling rates, either omitting or not proving accurate data on them, which seriously compromise their reproducibility. Others, however, have the disadvantage of rigid experimental conditions that implies controlled O_2, N_2 or SO_2 partial pressures at high temperatures (> 450ºC) for reaction times longer than 1 hour. Therefore, the development of a simple, fast, and cost-effective thermal treatment to carry out the effective oxidation of vanadium or vanadium oxide films for the fabrication of thermochromic VO_2 coatings has become a crucial issue.

In this paper, we report a simple and straightforward post-deposition oxidation strategy for the effective oxidation of DC magnetron-sputtered V or VO_x films to obtain thermochromic VO_2 (M1) nanostructured films of controlled crystallinity and grain size. Taking advantage of the great reactivity of these high surface-to-volume porous nanostructures, in addition to evaluate how oxidation occurs in systems of different morphology and composition, vanadium films were deposited by GLancing Angle Deposition (GLAD) whereas VO_x films were produced by combining GLAD and the Reactive Gas Pulsing Process (RGPP). Thanks to the accurate control of temperatures and reaction times, as well as heating rates, fast thermal treatment of these GLAD thin films was successfully performed in air atmosphere. Afterwards, all these oxidized systems were completely characterized by means of Raman spectroscopy, scanning electron microscopy (SEM) and scanning-transmission electron microscopy (S)TEM techniques, including high-angle annular dark-field (HAADF) and high-resolution (HRTEM) imaging, as well as electron energy-loss spectroscopy (EELS), allowing us to unravel the key role that reaction time plays not only in the selective generation of different vanadium oxide phases but also in the formation of VO_2 (M1) layers of a diverse nature, morphology and thickness. Likewise, the effect of oxygen injection times on the subsequent oxidation of the vanadium oxide GLAD films prepared by RGPP was also investigated. Finally, in order to evaluate the MIT response of such oxidized coatings, the surface work functions of the best thermally treated V or VO_x samples were investigated through Kelvin probe force microscopy (KPFM) measurements [33].

Materials and Methods

2.1. Deposition process

Films were deposited at room temperature by DC magnetron sputtering from a vanadium metallic target (51 mm diameter and 99.9 atomic % purity) in a homemade deposition chamber which was evacuated down to 10^{-5} Pa before each run by means of a turbomolecular pump backed by a primary pump. The target was sputtered with a constant current density J = 100 A m^{-2}. Single crystalline (100) silicon substrates were placed at 65 mm from the target surface. Porous V or VO_x films with large surface-to-volume ratios and enhanced sensitivity to oxidation were deposited by combining GLAD (GLancing Angle Deposition) and Reactive Gas Pulsing Process (RGPP). The following optimized conditions were used according to previous studies [24]. The incidence angle (α) of the incoming particle flux relative to the substrate normal was set at α = 85° with no rotation of the substrate (i.e., ϕ = 0 rev h^{-1}). Argon was injected at a mass flow rate of 2.40 sccm and the pumping speed was maintained at S = 13.5 L s^{-1}, whereas the oxygen gas was periodically supplied into the sputtering chamber. A rectangular pulsed signal was employed for the oxygen flow rate with regard to time evolution (Figure 1). The pulsing period was set at P = 16 s. The maximum oxygen flow rate was q_{O2Max} = 0.40 sccm. It corresponds to the critical flow required to avalanche the process in the compound sputtering mode. The minimum oxygen flow rate was q_{O2min} = 0 sccm. Thus, the injection time of the oxygen gas was changed from t_{ON} = 0 to 8 s. These operating conditions gave rise to a total sputtering pressure changing slightly in-between 3.00-3.08×10^{-3} mbar and target potential from 305 to 324 V, which do not disturb the growth mechanisms of the GLAD process (Table 1). It is worth noting that RGPP allows an alternation of the process between metallic and oxidized sputtering

modes. Such a precise alternation gives rise to a monotonous increase of the oxygen concentration in metal oxide films, and leads to tunable physico-chemical properties [34–37]. Deposition rate is influenced by the t_{ON} time as shown in Table 1. As previously noticed in former investigations [24,34,37], oxygen gas pulsing systematically produces a maximum of the deposition rate of metal oxide thin films when measured as a function of the t_{ON} time. This effect is mainly assigned to the periodic alternation of the reactive sputtering process between the metallic and the compound (poisoned target) sputtering mode, which occurs for a given range of t_{ON} times. In our study, the thickness of the vanadium film (t_{ON} = 0 s) was measured by profilometry, adjusting the deposition time to obtain a film thick enough (~700 nm) to investigate how the oxidation progresses when the subsequent thermal treatments are applied. This same deposition time was later fixed for films prepared with t_{ON} > 0 s.

2.2. Thermal treatments

After deposition, vanadium or vanadium oxide samples were thermally treated in a homemade reaction system consisting in an Al_2O_3 tube on a SiC resistors furnace able to reach 1500°C, with an attached concentric steel tube where a high-temperature steel covered k-type thermocouple inside which acts as an axle for a system of horizontal translation (for a more detailed overview of the reaction system, refer to Supplementary Material Section I). At the end of the metallic tube nearby the furnace, the thermocouple crosses and fixes to a cylinder placed inside this tube, mechanized with a hitch to hang a combustion boat. Thus, the thermometer tip is always placed some millimeters over the center of this alumina crucible, allowing the temperature in the reaction zone to be life-tracked. The other end side also crosses and is fixed to another piece that is part of a handlebar used to slide the specimen holders inside and outside. In this way, by fixing a

temperature in the center of the furnace, one is able to control the temperature increase (heating rate) by moving the boat more and more inside the furnace. Consequently, translation routines were prepared for reaching an average heating rate of 42ºC s^{-1}, as well as for adjusting longer or shorter reaction times at the desired temperature of 550ºC. Lastly, all the samples were cooled down in open-air atmosphere. It should be noted here that the choice of these thermal treatment conditions is grounded in an exhaustive preliminary study (which is currently in press) focused on the oxidation of pure vanadium nanoparticles of similar size to the nanocolumns within the film (100-200 nm) [38]. In this manner, the conditions that allowed to achieve higher VO_2 yields in nanoparticles were transferred to the oxidation of vanadium or vanadium oxide GLAD layers, leaving the reaction time as the only optimization variable.

2.3. Characterizations

Cross-sectional and plan-view scanning electron microscopy (SEM) images were acquired using FEI Nova NanoSEM and FEI Teneo microscopes operated at 5 kV, to examine the general morphology and size of each film. To obtain additional insights into the nanostructure of such systems, high-resolution transmission electron microscopy (HRTEM), selected area electron diffraction (SAED) and high-angle annular dark-field imaging (HAADF) studies were carried out in two TEM microscopes (FEI Talos F200X and JEOL 2100 LaB_6), working both at an accelerating voltage of 200 kV. A Gatan Imaging Filter (GIF) Continuum system fitted in the Talos microscope was used for spatially-resolved EELS analysis in scanning mode. STEM-EELS 2D spectrum image (SI) data were acquired using a 2.5 mm diameter aperture and 0.05 eV/channel energy dispersion. The convergence and collection semi-angles were set to 10.5 and 20.0 mrad, respectively, and the probe current was about 150 nA. In this

configuration, the energy resolution was 0.8 eV. In order to allow accurate chemical shift measurements, the Dual EELS mode was used to record nearly simultaneously both, low-loss, and V-$L_{2,3}$ in addition to O-K edges, at each pixel position. Dwell times of about 0.9 to 2 seconds per pixel were set to optimize the signal-to-noise ratio. Electron-transparent cross-sectional samples were prepared for TEM observations by means of both tripod polishing and focused ion beam (FIB) approaches. For this purpose, a tripod polisher (Model 590 Tripod Polisher®) was used to progressively thin the samples to a few microns, followed by Ar^+-ion milling in a Gatan PIPS system setting the acceleration energy of both guns to 3.5 keV (+7° top and −7° bottom). Alternatively, FIB lamellae were also prepared in a Zeiss Auriga FIB-SEM system.

Raman spectroscopy measurements were determined by using a dispersive Raman spectrometer (Jasco, model NRS7200) with a 100x objective coupled to a 532.19 nm NdYAG laser excitation source. Raman spectra were recorded with a spectral resolution of 1 cm^{-1} in the range of 39–856 cm^{-1}. These wavenumbers are those where vanadium oxides show their characteristic Raman bands. Care was taken to avoid heat-induced phase changes in the samples, so laser power was set at 0.6 mW and Raman spectra were collected for 30 s with an average accumulation of two spectra.

Finally, KPFM measurements at increasing and decreasing temperatures were performed with a Bruker MultiMode 8-HR AFM system, equipped with a water-refrigerated scanner (model AS-130VT), that included a variable-temperature sample stage connected to a MultiMode High Temperature Heater controller (maximum temperature 250°C) from Digital Instruments/Veeco. A specialized probe holder that fits to a silicone rubber seal to form a controlled environment space for the tip and the sample, was used to perform these measurements. The sample temperature was

previously calibrated by performing a heating/cooling experiment in which the sample was substituted by a K-type thermocouple glued with thermal paste to a metallic puck (similar to the one used to attach the sample to the scanner stage). Thus, the small difference between the scanner heater controller temperature and the real sample temperature can be easily estimated for every heating/cooling step. A specialized KPFM SiN probe from Bruker (type PFQNE-AL), with a nominal tip radius of 5 nm, was used to obtain both topographic, in the conventional tapping mode, and simultaneous surface potential images, in the Frequency Modulated-KPFM (FM-KPFM) mode. The work function of the tip was calibrated against gold using an Al/Au/Si test sample also from Bruker (reference PF-KPFM-SMPL) before and after the thermal cycle. Tip wearing during the KPFM experiment was minimum, as can be inferred from the fact that topographic images hardly show loss of lateral resolution, nor the probe work function changed significantly after the heating/cooling cycle was completed. It should be noted that, to ensure that the same sample area was scanned at each temperature, the tip had to be relocated on the sample surface at every temperature step, to compensate for the AFM scanner thermal drift.

Results and discussion

Characterization of as-deposited thin films

Pure vanadium or vanadium oxide GLAD thin films were deposited on silicon substrates at $\alpha = 85°$ and oxygen was pulsed during the deposition, varying the oxygen injection time (t_{ON}) from 0 to 8 s. In this regards, five samples were deposited which were tagged as V0 ($t_{ON} = 0$s), V2 ($t_{ON} = 2$ s), V4 ($t_{ON} = 4$ s), V6 ($t_{ON} = 6$ s), and V8 ($t_{ON} = 8$ s). For the purpose of exploring the structure and the morphology of as-deposited

thin films, Figure 2 shows cross-sectional and planar view SEM micrographs of samples V0 to V8. As can be seen, all samples exhibit a well-defined structure of inclined columns, but the effect of the oxygen injection time is also evidenced. As reference, sample V0 presents columns slightly connected to each other, which gives rise to a porous structure about 700 nm thick. Nonetheless, as oxygen injection time increases, samples gradually become thicker (since deposition rate increases as well [24]) and columns are more and more narrow, which not only promotes the connection between the columns but also leads to a decrease in the total porosity. This is clearly observed in Fig. 2, specially for planar view images, which were taken at the same magnification. Furthermore, it was also found that all samples presented column tilt angle (β) values lower than expected according to common empirical ballistic approaches such as the tangent [39] ($\beta = 80°$) and Tait [40] ($\beta = 58°$) rules. However, it has been proved that these empirical expressions have completely succeeded in accounting for the tilt angle of nanocolumns, when $\alpha < 50°$ [41], so that additional mechanisms, more complex than geometrical relationships, must be taken into account to understand the formation of such columnar structures. In general, it is assumed that the β angle value depends on the chemical nature of the deposited material, the deposition conditions, as well as well as the characteristics of the deposition reactor itself [42,43]. In addition, experimental studies as well as simulations show that during the first growing stages (a few nanometers thick), initial nuclei produce small columns, which are perpendicular to the substrate [44,45]. These microscopic islands create a shadowing effect, which is magnified by the oblique angle deposition. Particles impinging on the growing film can only reach a partial area of the columns apex (in front of the particle flux) and a further increase of the deposition leads to a tilting of the columns up to a given angle β. The

latter depends on many parameters such as the chamber geometry, the sputtering pressure, growth kinetics, self-diffusion of sputtered particles and so on. Likewise, a progressive decrease of the β angle can also be observed as oxygen injection time increases (see Supplementary Material Section II), which can be linked to the mean free path of the sputtered particles. The sputtering pressure, which increases with oxygen injection time, promotes the collisions between particles, leading to the widening of incoming the particle flux from the target in its pathway toward the substrate. This phenomenon can give rise to maximum column angles β close to 20–30° for high incident angles, which could explain the effect observed here for RGPP samples [24].

Additionally, with the aim of disclosing the crystal structure, the predominant phases present in the as-deposited films, and hence the effect of oxygen injection time, V0 and V8 samples were prepared for TEM observations. Figures 3(a) and (b) display the STEM-HAADF images of samples V0 and V8, respectively. As can be appreciated, the V0 overlayer presents a more porous structure when compared to that of V8, which is in agreement with the evidences stated before. Also noteworthy is the great difference between the β values for both samples, being indeed double for the non-oxidized one (β = 52 ° for V0, and β = 26 ° for V8). Besides, HRTEM images and their fast Fourier transform (FFT) for the top regions of samples V0 (Fig. 3(c)) and V8 (Fig. 3(d)) evidenced a remarkable difference between both samples at the nanoscale. On one side, the HRTEM studies not only demonstrate that the vanadium GLAD layer (V0) is crystalline after deposition at room temperature but also it is mainly composed by the pure vanadium cubic phase. By contrast, the vanadium oxide GLAD layer (V8) presents a less crystalline structure, which could be explained by an enhanced atomic peening effect (i.e. the bombardment of the growing film by energetic backscattered ions and

sputtered particles) that can generate a greater amount of structural defects [46]. Indeed, as the oxygen injection time increases up to t_{ON} = 8 s, the average voltage of the vanadium target rises, resulting in an increase of the mean energy of the Ar ions impinging on the target (Table 1). Consequently, the particles reaching the substrate (backscattered Ar and sputtered particles) are expected to be more energetic in the case of the V8 film, generating more damage in its structure. Moreover, the HRTEM micrograph and its FFT (equivalent to a diffractogram of the crystalline structure) for sample V8 revealed interplanar distances and angles proper from those of the tetragonal $V_{16}O_3$ phase. Lastly, in order to check more extended regions than those inspected by HRTEM, selected area electron diffraction (SAED) patterns were collected for V0 and V8 samples (see Supplementary Material Section III) which, in addition to support the greatest crystallinity of sample V0, confirmed that the major phase in V0 sample was cubic vanadium (AMCSD 0011235) whereas the V8 sample was constituted by a mixture of cubic VO (ICDD 01-075-0048) and tetragonal $V_{16}O_3$ (ICDD 04-011-0169).

Thermal oxidation and subsequent characterization of pure vanadium films

Once disclosed the nature, morphology and structure of the as-deposited vanadium or vanadium oxide GLAD films, their fast heating was conducted to promote the formation of the VO_2 thermochromic phase. Note that, initially, only sample V0 was thermally treated since the aim of this first stage was to optimize reaction times that maximize the amounts of VO_2. In all cases, the reaction temperature (T_r) and heating rate (h_r) were fixed to 550ºC and 42ºC s^{-1}, respectively. In this light, the V0 sample was subjected to different reaction times (t_r) ranging from 1 to 300 seconds followed by the subsequent instantaneous cooling in air. A detailed scheme of the fast thermal treatment process can

be found in Figure 4(a). Here, with the aim of demonstrating the high control achieved in our developed system, it is worth mentioning that all the displayed temperature versus time tracks are those recorded during the thermal treatment. Thereupon, Raman spectroscopy analyses were performed on all the treated samples for the purpose of monitoring the rise of the different vanadium oxidized phases as reaction time increases. Fig. 4(b) shows the Raman spectra collected for V0 samples heated at 550ºC and subjected to different reaction times (from 1 to 300 seconds). As seen, Raman signals given for samples treated during 1 and 15 seconds can be characterized, in addition to be quite noisy, to contain weak VO_2 (M1) peaks at ~194, 224, 262 and 612 cm^{-1}, as well as others at ~304 and 420 cm^{-1} which can be associated to the presence of VO_x ($1.67 < x < 2$) compounds [47]. The remaining Raman bands found in both samples might be attributed to metastable vanadium oxides whose Raman scattering data have not been reported yet. As reaction time increases, VO_2 (M1) Raman signature gradually becomes more significant, reaching a pure VO_2 (M1) signal for $t_r = 45$ s which perfectly matches with other Raman VO_2 spectra previously reported in the literature [47–50]. From this point forward, longer reaction times would only promote the formation of the α-V_2O_5 phase (according to Ref. [47]), turning into the predominant phase for $t_r > 75$ s. Thus, all of the above points out the fundamental role that the precise control of the thermal treatment parameters, and very specially the reaction time, plays in achieving the effective transformation of V into VO_2 (M1) thin films.

Furthermore, the structure and morphology of all these annealed samples were also explored by means of SEM. Figure 5 illustrates the top views of all the thermally treated V0 samples which not only allow to identify the different stages involved in the oxidation of such layers but also bring to light some characteristic features of both VO_2

and V_2O_5 phases. Here, a progressive widening of the grain size for reaction times between 1 and 45 seconds can be observed (for a more detailed overview of the grain morphology after 1 and 15 seconds reaction times, refer to Supplementary Material Section IV). Hence, it seems that the oxidation of vanadium GLAD V0 occurs from the top to the bottom of the layer, starting with the formation of small nuclei of VO_x ($x < 2$) that will later evolve into coarser grains of VO_2 (M1). Likewise, it also appears that the slanted columnar morphology so characteristic of the GLAD systems, which is the main responsible for the almost instantaneous and efficient oxidation of these films thanks to its large surface-to-volume ratios, is lost after thermal treatment. On the other hand, it is also noticed that $t_r > 60$ leads to the gradual growth of these grains along the axial direction, emerging a kind of micro-rods structure randomly distributed in all directions which is characteristic of the V_2O_5 [51,52]. In consequence, the porosity of the film increases again, but at the expense of its consistency and homogeneity.

In order to accomplish a comprehensive characterization of the fast thermally treated V0 samples, as well as to reinforce the assumptions previously made, TEM studies were performed on several selected samples. Figure 6(a), (b) and (c) display the bright-field TEM cross-sectional views for V0 samples after reaction times of 1, 45 and 300 seconds, respectively. In Fig. 6(a), two clear regions are distinguished: a first compact layer of about 120 nm thick composed by well-defined grains (to have a better insight of this first layer, refer to Supplementary Material Section V), and a second porous and thicker layer beneath (~ 520 nm) that preserves the GLAD morphology of the original system. This confirms the previous hypothesis that oxidation initiates on the surface of the film and progresses towards the substrate as the reaction time increases. Similarly, it is also evidenced that the GLAD morphology disappears as the oxidation of the film

develops. Fig. 6(d) shows a HRTEM micrograph of a grain corresponding to the oxidized region (sublayer 1) of the V0 sample for t_r = 1 s, revealing atomic columns of monoclinic VO_2 (M1) (ICCD 04-005-4338) oriented in the [011] zone axis, with families of planes and their parameters and angles highlighted. Thus, it could be asserted that the granular reaction product that progresses from the surface of the layer towards the substrate is the thermochromic VO_2 phase. The same applies to the V0 sample subjected to a reaction time of 45 seconds, although the size of the grains observed here, as well as the thickness of the oxidized layer (~ 400 nm), are both significantly greater (Fig. 6(b)). Note that the reduced thickness of the V0 sample for t_r = 45 s is not directly associated to thermal treatment itself, but rather to an excessive ion-milling during the FIB sample preparation. Nonetheless, this fact does not prevent the observance of what appears to be an oxidation gradient characterized by larger grains in regions near the surface which progressively decrease in size as oxidation progresses towards inner regions. In this way, it seems that, until the 45-second reaction time is reached, the oxygen in-diffuses more and more, giving rise to an overall appearance of bigger and single-crystalline VO_2 grains. The above could explain the outstanding Raman VO_2 (M1) signal acquired for this sample. Likewise, the HRTEM images collected in this oxidized region (sublayer 1 of the V0 sample for t_r = 45 s) also show interplanar spacings and angles that match with the $[11\bar{2}]$ VO_2 (M1) orientation (Fig. 6(e)). Nonetheless, an unreacted buried layer of about 160 nm thick still remains. Overall, it must be highlighted that, for $t_r \leq 45$ s, homogeneous oxide layer thicknesses are generated, whereas the original total thickness of the layer is not significantly affected. Also note that the VO_2 thicknesses attained here (120 – 400 nm) are above those conventionally reported in the literature for optical applications in thermochromic

smart windows [3,4,10,53]. Hence, the subsequent thermal treatments of thinner (< 100 nm) vanadium GLAD films at T_r = 550ºC, h_r = 42ºC s^{-1} and $t_r \leq 45$ s, could lead to the exclusive formation of pure VO_2 films of controlled grain size, which has been reported to have significant effects on the features of the MIT transition [54], thanks to the precise control of reaction times.

On the contrary, the V0 sample subjected to t_r = 300 s presents a structure quite different from those previously visualized (Fig. 6(c)). In this case, a unique layer can be distinguished, being its thickness almost three times thicker than the previous ones. This is clearly linked to an advanced oxidation of the film characterized by the oxygen enrichment, which leads us to think that V_2O_5 is the predominant compound in the sample. Indeed, the HRTEM image displayed in Fig. 6(f), which was collected from a representative region of V0 sample for t_r = 300 s, confirms this assumption since characteristic lattice distances and angles of the [012] V_2O_5 zone axis (ICDD 04-008-4555) were identified. Other features of this sample are the irregular shapes and thicknesses as well as the presence of big voids (see Supplementary Material Section VI), which could all compromise the consistency of the coating.

In order to go a little further in the characterization of such thermally treated samples, as well as to unravel the vanadium oxidation state within each of the layers previously distinguished, STEM-EELS analyses were carried out in V0 preparations subjected to t_r = 1, 45 and 300 s. Like in others 3d transition metals, the $L_{2,3}$ edge of vanadium exhibits a characteristic shape consisting in two sharp peaks usually separated by a few eV (known as “white lines”). Since those major features are due to electron transitions from 2p ($2p_{3/2}$ and $2p_{1/2}$, for L_3 and L_2, respectively) to unoccupied 3d states, the L_3/L_2 intensity ratio as well as the shift of the $L_{2,3}$ lines reveal the d-band occupancy, and

consequently they are very sensitive to the valence state of the metal [55,56]. As a general trend, and especially in the case of V, an increase in the oxidation state leads to a shift of the $L_{2,3}$ edge towards higher energy loss as well as a decrease of the L_3/L_2 ratio [57–59]. Because the oxygen K-edge reflects the local density of states at the oxygen site, changes in its energy-loss near-edge structure can also be considered to determine the oxidation levels. In the case of the V-O system, the O-K edge overlaps with the continuum region of V-$L_{2,3}$ edge, which hinders chemical quantification. However, monitoring the relative band shift between O-K and V-L_3 edges as well as the shape of the O-K edge, in particular modifications in the relative intensities of the e_g and t_{2g} pre-edge peaks can be insightful to reveal some changes of the V valence [60,61].

Figure 7 displays the extracted EELS signals containing both the V-$L_{2,3}$ and O-K pre-edge which were summed in small characteristic areas of V0 samples thermally treated at h_r = 42ºC s^{-1}, T_r = 550ºC, and t_r = 1, 45 and 300 s. For detailed information on the processing of the STEM-EELS 2D spectrum image datasets, see Supplementary Material Section VII. As can be seen in Fig. 7(a), the EELS spectrum #1a collected from just one individual nanocolumn (brighter contrast on the HAADF image) is characteristic of metallic vanadium, since only the V-$L_{2,3}$ white lines separated by ΔE_L = 7.0 eV, with the L_3 peak located at 514.1 eV, are visible. Also note that peak positions and energy differences extracted from these and subsequent EELS spectra can be found in Table S1 (Supplementary Material Section VII). Between two nanocolumns, the EELS signal shows some modifications (spectrum #2a) since the $L_{2,3}$ lines are shifted towards the higher energies (L_3 position at 514.8 eV) and a single peak around 531.7 eV appears in the O-K pre-edge region. This feature is attributed to the e_g state arising from hybridization between O 2p and V 3d states [60,61]. Those observations, combined with

the fact that the measured energy difference between the e_g and the V-L_3 peaks is ΔE = 16.9 eV, may reveal the V^{2+} valence state (VO) [59,62]. This indicates that, despite the V nanocolumns are mostly metallic, they may present a slightly oxidized surface due either to air exposure, as evidenced in other GLAD systems [63], or to the thermal annealing process itself. In the upper region of the film, measurements as the spectrum #3a shows more pronounced changes characterized by a higher energy shift of the V-$L_{2,3}$ lines (L_3 position at 516.0 eV) and by the presence of two peaks in the O-K pre-edge region that corresponds to t_{2g} (around 528.6 eV) and e_g (around 530.8 eV) states coming from the O 2p and V 3d hybridization [60,61]. This increased shift of V-$L_{2,3}$ lines, but also the stronger t_{2g} contribution relative to e_g, the reduced energy difference between the e_g and the V-L_3 line (ΔE=14.7 eV) as well as the strong shoulders visible on the left sides of the L_3 and L_2 peaks (shown by the arrows) are fingerprints that allow to confirm the V^{4+} valence state (VO_2) [58,59].

When the annealing time increases up to 45 s (Fig. 7(b)), it is observed that the distribution of the oxidation states within the layer remains quite close to the previous case, but with a much deeper oxidized layer that extends up to about 400 nm from the surface. The aforementioned oxidation gradient can be more easily appreciated here: a first homogeneous overlayer of about 250 nm formed by larger grains, and a second inner sublayer (~150 nm thick) composed by smaller grains of different sizes are distinguished. The EELS signals obtained in the upper part (spectrum #3b, where large grains are observed) and in the lower part (spectrum #2b, where both smaller grains and voids are observed) of this layer present very similar features than for the spectrum #3a (also see Table S1), confirming that the greater part of the films is in the V^{4+} valence state in agreement once again with the presence of VO_2. At the bottom part of the film

(spectrum #1b), within about the first 160 nm of the layer, the EELS signals are quite similar to those of spectrum #2a, characteristic of a V^{2+} valence state.

By contrast, as evidenced in Fig. 7(c), 300 s reaction time leads to a complete modification of the oxidation state in the whole layer. All the EELS signals corresponding to regions located at different thicknesses within the coating present the same features that matches very well with a V^{5+} valence state (V_2O_5) according to the trends evidenced in the literature. As compared with the EELS signals of the previously identified VO_2 regions, the spectra shown in Fig. 7(c) present on the one hand V-$L_{2,3}$ white lines that are slightly shifted (0.5 eV) towards higher energies (L_3 position at about 516.6 eV), and on the other hand less separated O-K pre-edge peaks with a stronger t_{2g} contribution [58,59,61,64]. We can also mention that two weak shoulders are detected on the left side of the V-L_3 peak, indicating the presence of the vanadium pentoxide.

Thermal oxidation and subsequent characterization of vanadium oxide films

Once known how oxidation develops for pure vanadium GLAD films, it is time to explore how VO_x GLAD films deposited at different oxygen injection times behave when subjected to fast thermal treatments. In this way, provided the good outcomes obtained for the V0 sample, a thermal treatment consisting in a fast heating ramp of 42ºC s^{-1}, followed by keeping a constant temperature of 550ºC for 45 seconds, and a final cooling down in air atmosphere, was systematically applied to V2, V4, V6 and V8 samples. Figure 8 shows the planar view SEM images obtained for V2, V4, V6 and V8 samples after thermal treatments. As can be seen, all these samples present a granular structure quite similar to those presented in the V0 sample subjected to t_r = 45 s.

However, remarkable differences are noticed. Proof of this is the undesired appearance, to a greater (samples V4 and V8) or lesser (samples V2 and V6) extent, of V_2O_5 micro-rod bundles on the surface, as well as the cracking (sample V6) or the final detachment (sample V8) of the coating (for a more detailed perception of such cracks and delaminations, refer to Supplementary Material Section VIII). Note that the detachment of the V8 overlayer took place while it was cooled down in air. Thus, this phenomenon could be associated to the combined effect of the two following events. On the one hand, it should not be forgotten that, as oxygen injection times increases, columns become taller and narrower, so the development of a more compact layer over such porous structures can result in a greater source of stress. Likewise, it should also be kept in mind that the phases present in the sample V8 before the thermal treatment (VO and $V_{16}O_3$) were not the same as for sample V0. Thus, all this could lead to the outbreak of residual stresses at the different interfaces, probably favored by thermal expansion mismatches between layers, which can result in the development and propagation of cracks or, in the worst case, in the collapse of the physisorbed film, promoting the observed lack of adherence.

Figure 9(a) reveals the Raman spectroscopy studies carried out on V2, V4 and V6 samples. Note that Raman analyses could not be performed on the V8 sample as result of its detachment. The measured Raman spectra for V2 and V6 samples clearly show the characteristic Raman bands of the VO_2 (M1) phase together with a weak band at around ~340 cm^{-1} which is associated to the presence β-V_2O_5 [47]. By contrast, the Raman spectrum of the V4 sample not only indicates a clear VO_2 (M1) signature, but also a prominent signal of two overlapped bands at ~266 and 269 cm^{-1} which are characteristic to γ'-V_2O_5 and ε'-V_2O_5 pentoxide polymorphs [47]. All this agrees with

the previously observed through SEM studies, which noticed the presence of the so characteristic V_2O_5 micro-rods, especially for the V6 sample. Therefore, in addition to the cracking and the detachment of the film, it seems that the thermally treated vanadium oxide GLAD samples also have the disadvantage of being less homogeneous than the V0, with the appearance of V_2O_5 micro-rod bundles on the surface. Notwithstanding, the results obtained for the V2 sample are quite promising.

So as to ultimately know how oxidation develops along the thickness of such porous vanadium oxide films, it was decided to explore the two most favorable samples so far, i.e., V2 and V6 samples, by means of TEM methods. Fig. 9(b) and (c) illustrate the cross-sectional bright-field overviews of V2 and V6 samples, respectively. In the same way as happened for sample V0, both samples clearly present three regions: a first sublayer located in the top part of the films (sublayer 1) characterized by large and single-crystalline grains; an intermediate region beneath (sublayer 2) consisting of grains of considerably smaller size; and a third most buried region (sublayer 3), in principle not oxidized, that preserves the features of the GLAD structures. Therefore, it seems that the arising of this oxidation gradient is not ultimately linked to the deposition approach, but to the nature of the thermal treatment itself. Overall, some distinguishing characteristics of these two samples are a thicker first sublayer (~ 390 nm) for the V2 sample versus a greater intermediate thickness sublayer (~ 360 nm) for the sample V6. However, the size of the grains located in the so-called sublayer 1 of both samples is considerably bigger than those formed in the V0 sample for the same thermal treatment. Likewise, the oxidized layer thicknesses of V2 and V6 samples are ~ 570 nm and ~ 680 nm, respectively, which means that vanadium oxide GLAD films are more prone to oxidation than those of pure vanadium. All this could be explained by the fact that taller

and smaller diameter columns, which is favored as oxygen injection time increases, imply greater surface-to-volume ratios, thus increasing the reactivity of the coating [63]. For this same reason, oxidation was more effective and progressed deeper in sample V6 than in V2. Instead, it should also be noticed that the original thickness of as-deposited V2 and V6 samples was not significantly affected after oxidation. In addition to the above, the HRTEM images collected from large-sized grains of V2 and V6 samples (Supporting Information Section IX) once more demonstrated the presence of the thermochromic VO_2 (M1) phase in the most surface layers.

In order to completely understand the effect that the deposition conditions can have on the oxidation process, and in particular the pulsed injection of oxygen, STEM-EELS analyses were also carried out in V2 and V6 oxidized samples as those shown in Figure 10(a) and (b), respectively. The EELS signals (see also Table S1 for more details) collected from the bottom part of the films, where the GLAD nanocolums are still visible, are similar and match well with a metallic V or poorly oxidized vanadium (VO), whereas the top part of the films reveal features that are clear fingerprints of VO_2. In the case of the V2 film, it is important to note that a thin intermediate sublayer (about 80 nm) has been identified on top of the nanocolumns, which shows EELS signal (spectrum #2 on Fig. 10(a)) with intermediate features (white line shift, energy difference ΔE, O-K pre-edge peak shapes) compared to VO and VO_2 and that matches with V^{3+} (V_2O_3) valence state according to the literature [58,62]. As a general trend, it can be observed that, as oxygen injection time increases more heterogeneous and thicker VO_2 layers are achieved after oxidation: greater oxygen injection times, in addition to partially oxidize the film, give rise to the formation of apparently less porous structures but with higher surface areas, which enhances the reactivity of the system.

However, as evidenced through Raman and EELS studies, they may develop V_2O_5 or V_2O_3 oxides up or down, respectively. Thus, it seems that a gradient of phases from more (V^{5+}) to less (V^{3+}) oxidized states, with an intermediate majoritarian V^{4+} valence region, following the V-O phase diagram trend [47], is developed along the film thickness in the direction from the surface (continuously exposed to O reactivity) to the interface with the substrate (where events promoted by O diffusion are more limited).

Metal-to-insulator response of the oxidized films

Finally, with the aim of evaluating the MIT of the oxidized samples, variable temperature KPFM was used to obtain the evolution of the work function (W_S) maps with temperature. Figures 11(a) and (b) show the overlayed tridimensional images of topography and work function for the V0 sample subjected to t_r = 45 s at two different temperatures, below and above the MIT. In Fig. 11(c) the distribution of W_S values in both images, calculated from the KPFM values considering the tip work function, are represented. These values are fitted to a Gaussian function and, from the mean values found (peaks), it is clearly shown that a reduction in work function of about 0.16 eV takes place, as expected for this kind of transition [33,65].

A more detailed study was performed for the oxidized V2 sample (550ºC, h_r = 42ºC s^{-1} and t_r = 45 s), as shown in Figure 12, by scanning a 2 × 2 μm^2 area of this sample during a full heating and cooling cycle. The topography of this region is shown in Fig. 12(a), from which a RMS roughness value of S_q = 17.4 nm is obtained. On the other hand, Figs. 12(b)-(f) display the evolution of the work function maps with temperature during the heating/cooling cycle. These maps were derived from the KPFM images, taking into account the work function of the tip, and from them, the W_S distribution histograms can

be represented and fitted to a Gaussian function (i.e., a normal distribution is again considered). The mean W_S values obtained at each temperature are represented in Fig. 12(g). Here, error bars length corresponds to the standard deviation of each Gaussian distribution fit. As expected, a hysteretic MIT, manifested as a reduction in work function of ~0.2 eV, which is considerably greater than those reported in the literature to date for VO_2 thin films (0.10-0.15 eV) [33,65], is clearly shown, with inflection points at around 78°C during heating and at around 73°C during cooling, and thus a thermal hysteresis width about $\Delta T \sim 5°C$. Although MIT temperature is 68ºC for pure single-crystalline M1 phased VO_2, different transition temperatures ranging from 40ºC to 85ºC have been found, even in similarly grown thin films, depending on deposition conditions and postprocessing [66]. In this regard, it has been reported that the increase in the MIT temperature can be a consequence of the residual strain along the *c*-axis of VO_2 [67], as well as of the adsorption of oxygen atoms [68].

In the same vein, it has been also evidenced that the work function of VO_2 is greatly influenced by oxygen non-stoichiometry [65,68], so that oxygen atoms can induce an increase in the work function values. Thus, oxygen adsorption must play a role in the MIT measured using KPFM in air atmosphere, since some oxygen atoms may be adsorbed at low temperature, then desorbed, at least partially, during the heating, and re-adsorbed on cooling, influencing the value of the MIT drop observed. Nevertheless, the work function drop obtained here is still lower than the value (~0.35 eV) calculated by Chen et al. [68], which is more than acceptable, considering the environmental conditions. In any case, these results demonstrate the existence of a MIT in the thermally treated samples. Furthermore, although it is true that V2 sample was subjected to a single heating-cooling cycle, it apparently shows a good repeatability of

the thermochromic behavior, which has been proved to be crucial for practical applications [69].

In view of the foregoing, it is clearly demonstrated that the controlled and fast oxidation of V or VO_x GLAD films in air atmosphere leads to the attainment of promising VO_2 thermochromic layers. Hence, given the VO_2 thicknesses achieved here for the different fast thermal treatments carried out, it is thought that the deposition and subsequent oxidation of vanadium or vanadium oxide GLAD film thicknesses similar to those required for optical applications in smart windows (< 100 nm) would give rise to the exclusive formation of VO_2 (M1) layers of adjustable grain size (to see an overview of the different mean VO_2 grain sizes achieved in this study, refer to Table 2) and crystallinity by controlling (a) oxygen injection times during deposition ($t_{ON} \leq 2$ s); and (b) reaction times ($t_r \leq 45$s) for thermal treatments conducted at 550ºC and $h_r = 42$ºC s^{-1}. In fact, these latest assumptions, which should be also contrasted through optical and electrical measurements, will be the focus of our future investigations.

Conclusions

In this work, a novel, simple and cost-effective approach for the fast oxidation of vanadium-based films to accomplish thermochromic VO_2 coatings of tunable grain size and crystallinity has been reported. For this purpose, porous V or VO_x layers were prepared by DC magnetron sputtering involving the glancing angle deposition (GLAD) and the reactive gas pulsing process (RGPP), keeping deposition angle $\alpha = 85°$ and pulsing the oxygen gas with t_{ON} = 0, 2, 4, 6 and 8 s. As a first step, thanks to the accurate control of the oxidation parameters as well as the great reactivity of the high surface-to-volume deposited films, the fast oxidation of pure vanadium samples was

performed in air atmosphere at h_r = 42ºC s^{-1} and T_r = 550ºC, for reaction times (t_r) ranging from 1 to 300 s. Results collected for such oxidized systems through SEM and Raman spectroscopy not only allowed to explore the characteristic structure and morphology of the different oxide phase generated but also to optimize reaction times which maximize the highest amounts of the thermochromic VO_2 phase. Further TEM and STEM-EELS studies disclosed that $t_r \leq 45$ s guarantee the exclusive formation of VO_2 (M1) superficial layers of different grain size and crystallinity with thicknesses between 120 – 400 nm.

By virtue of the foregoing, the subsequent fast oxidation of vanadium oxide samples was carried out at h_r = 42ºC s^{-1}, T_r = 550ºC, and t_r = 45 s. Samples deposited with oxygen injection times $t_{ON} \geq 6$ s not only evidenced the cracking and film detachment but also an earlier formation of V_2O_5 microrods on the surface in addition to the VO_2 (M1) phase. The best results were obtained for the oxidized sample deposited with t_{ON} = 2 s, which showed the formation of VO_2 (M1) multilayers of about 570 nm total thick: the most superficial layer is composed by larger and single-crystalline VO_2 grains, whereas the second inner layer is characterized by smaller grains.

Finally, the remarkable surface potential drops recorded by temperature dependent KPFM measurements of the best thermally treated vanadium or vanadium oxide samples confirmed the outstanding and promising MIT response of the resultant VO_2 (M1) films. Therefore, it is determined that the post-deposition oxidation of < 100 nm thick vanadium-based samples deposited at $\alpha = 85°$ and $t_{ON} \leq 2$ s can lead to the exclusive formation of VO_2 (M1) coatings of adjustable grain size and crystallinity when the subsequent fast thermal treatments are conducted in air atmosphere using optimized conditions (h_r = 42ºC s^{-1}, T_r = 550ºC, $t_r \leq 45$ s).

CRediT author statement

Antonio J. Santos: Conceptualization, Methodology, Validation, Investigation, Writing - Original Draft, Writing - Review & Editing, Visualization, Funding acquisition.

Bertrand Lacroix: Software, Validation, Investigation, Formal analysis, Writing - Review & Editing, Funding acquisition.

Manuel Domínguez: Validation, Investigation, Resources, Writing - Review & Editing.

Rafael García: Resources, Supervision, Funding acquisition.

Nicolas Martin: Conceptualization, Investigation, Resources, Writing - Review & Editing.

Francisco M. Morales: Conceptualization, Methodology, Validation, Investigation, Resources, Writing - Review & Editing, Supervision, Project administration, Funding acquisition.

mmc1 docx

mmc2.docx

Declaration of Competing Interest

the author declare that they have no known competing financial interests or personal relationships that could have appeared to influence the work reported in this paper

ACKNOWLEDGEMENTS

A. J. Santos would like to thank the IMEYMAT Institute and the Spanish Ministerio de Educación y Cultura for the concessions of grants (ICARO-173873 and FPU16-04386). The "Talent Attraction Program" of the University of Cádiz is acknowledged by supporting B. Lacroix contract code E-11-2017-0117214. University of Cádiz and IMEYMAT are also agreed by financing the mutual facilities available at the UCA R&D Central Services (SC-ICYT), the UCA projects reference "PUENTE PR2018-040" and "PUENTE PR2020-003", and the IMEYMAT project references "LÍNEAS PRIORITARIAS PLP2019120-3 and PLP2021120-1". This work was supported by the

Spanish State R&D project (Retos y Generación de Conocimiento) ref. PID2020-114418RB-I00. The regional government of Andalusia with FEDER cofunding also participates through the projects AT-5983 Trewa 1157178 and FEDER-UCA18-10788. M. Domínguez acknowledges financial support from the Spanish Ministerio de Ciencia e Innovación under project reference EQC2018-004704-P FEDER 2014-2020, "Modernización del Servicio de Microscopía de Fuerza Atómica (AFM) del IMEYMAT".

REFERENCES

[1] J.B. Goodenough, The two components of the crystallographic transition in VO_2, J. Solid State Chem. 3 (1971) 490–500. doi:10.1016/0022-4596(71)90091-0.

[2] V. Devthade, S. Lee, Synthesis of vanadium dioxide thin films and nanostructures, J. Appl. Phys. 128 (2020) 231101. doi:10.1063/5.0027690.

[3] S. Wang, M. Liu, L. Kong, Y. Long, X. Jiang, A. Yu, Recent progress in VO_2 smart coatings: Strategies to improve the thermochromic properties, Prog. Mater. Sci. 81 (2016) 1–54. doi:10.1016/j.pmatsci.2016.03.001.

[4] K. Liu, S. Lee, S. Yang, O. Delaire, J. Wu, Recent progresses on physics and applications of vanadium dioxide, Mater. Today. 21 (2018) 875–896. doi:10.1016/j.mattod.2018.03.029.

[5] T.C. Chang, X. Cao, S.H. Bao, S.D. Ji, H.J. Luo, P. Jin, Review on thermochromic vanadium dioxide based smart coatings: from lab to commercial application, Adv. Manuf. 6 (2018) 1–19. doi:10.1007/s40436-017-0209-2.

[6] J.-P. Pouget, Basic aspects of the metal–insulator transition in vanadium dioxide

VO_2: a critical review, Comptes Rendus Phys. 22 (2021) 37–87. doi:10.5802/crphys.74.

[7] H. Lu, S. Clark, Y. Guo, J. Robertson, The metal-insulator phase change in vanadium dioxide and its applications, J. Appl. Phys. 129 (2021) 240902. doi:10.1063/5.0027674.

[8] C. Batista, V. Teixeira, J. Carneiro, Structural and morphological characterization of magnetron sputtered nanocrystalline vanadium oxide films for thermochromic smart surfaces, J. Nano Res. 2 (2008) 21–30. doi:10.4028/www.scientific.net/JNanoR.2.21.

[9] X. He, C. Gu, F. Chen, X. Xu, Vanadium dioxide thin films for smart windows: optical design and performance improvement, Eighth Int. Conf. Thin Film Phys. Appl. 9068 (2013) 90680G. doi:10.1117/12.2054369.

[10] Z. Chen, Y. Gao, L. Kang, J. Du, Z. Zhang, H. Luo, H. Miao, G. Tan, VO_2-based double-layered films for smart windows: Optical design, all-solution preparation and improved properties, Sol. Energy Mater. Sol. Cells. 95 (2011) 2677–2684. doi:10.1016/j.solmat.2011.05.041.

[11] N. Shen, S. Chen, R. Huang, J. Huang, J. Li, R. Shi, S. Niu, A. Amini, C. Cheng, Vanadium dioxide for thermochromic smart windows in ambient conditions, Mater. Today Energy. 21 (2021) 100827. doi:10.1016/j.mtener.2021.100827.

[12] B.G. Chae, H.T. Kim, D.H. Youn, K.Y. Kang, Abrupt metal-insulator transition observed in VO_2 thin films induced by a switching voltage pulse, Phys. B Condens. Matter. 369 (2005) 76–80. doi:10.1016/j.physb.2005.07.032.

[13] S.A. Corr, M. Grossman, J.D. Furman, B.C. Melot, A.K. Cheetham, K.R. Heier, R. Seshadri, Controlled reduction of vanadium oxide nanoscrolls: Crystal

structure, morphology, and electrical properties, Chem. Mater. (2008) 6396–6404. doi.org/10.1021/cm801539f.

[14] T. Driscoll, H.T. Kim, B.G. Chae, B.J. Kim, Y.W. Lee, N.M. Jokerst, S. Palit, D.R. Smith, M. Di Ventra, D.N. Basov, Memory metamaterials, Science. 325 (2009) 1518–1521. doi:10.1126/science.1176580.

[15] A.K. Prasad, S. Amirthapandian, S. Dhara, S. Dash, N. Murali, A.K. Tyagi, Novel single phase vanadium dioxide nanostructured films for methane sensing near room temperature, Sens. Actuator B-Chem. 191 (2014) 252–256. doi:10.1016/j.snb.2013.09.102.

[16] A. Perucchi, L. Baldassarre, P. Postorino, S. Lupi, Optical properties across the insulator to metal transitions in vanadium oxide compounds, J. Phys. Condens. Matter. 21 (2009) 323202. doi:10.1088/0953-8984/21/32/323202.

[17] M.G. Krishna, Y. Debauge, A.K. Bhattacharya, X-ray photoelectron spectroscopy and spectral transmittance study of stoichiometry in sputtered vanadium oxide films, Thin Solid Films. 312 (1998) 116–122. doi:10.1016/s0040-6090(97)00717-7.

[18] E. Hryha, E. Rutqvist, L. Nyborg, Stoichiometric vanadium oxides studied by XPS, Surf. Interface Anal. 44 (2012) 1022–1025. doi:10.1002/sia.3844.

[19] M.M. Seyfouri, R. Binions, Sol-gel approaches to thermochromic vanadium dioxide coating for smart glazing application, Sol. Energy Mater. Sol. Cells. 159 (2017) 52–65. doi:10.1016/j.solmat.2016.08.035.

[20] H. Liu, O. Vasquez, V.R. Santiago, L. Diaz, A.J. Rua, F.E. Fernandez, Novel pulsed-laser-deposition - VO_2 thin films for ultrafast applications, J. Electron. Mater. 34 (2005) 491–496. doi:10.1007/s11664-005-0056-y.

[21] Y.L. Wang, X.K. Chen, M.C. Li, R. Wang, G. Wu, J.P. Yang, W.H. Han, S.Z. Cao, L.C. Zhao, Phase composition and valence of pulsed laser deposited vanadium oxide thin films at different oxygen pressures, Surf. Coat. Technol. 201 (2007) 5344–5347. doi:10.1016/j.surfcoat.2006.07.087.

[22] R. Binions, G. Hyett, C. Piccirillo, I.P. Parkin, Doped and un-doped vanadium dioxide thin films prepared by atmospheric pressure chemical vapour deposition from vanadyl acetylacetonate and tungsten hexachloride: The effects of thickness and crystallographic orientation on thermochromic properties, J. Mater. Chem. 17 (2007) 4652–4660. doi:10.1039/b708856f.

[23] J. Du, Y. Gao, H. Luo, L. Kang, Z. Zhang, Z. Chen, C. Cao, Significant changes in phase-transition hysteresis for Ti-doped VO_2 films prepared by polymer-assisted deposition, Sol. Energy Mater. Sol. Cells. 95 (2011) 469–475. doi:10.1016/j.solmat.2010.08.035.

[24] V. Collado, N. Martin, P. Pedrosa, J.Y. Rauch, M. Horakova, M.A.P. Yazdi, A. Billard, Temperature dependence of electrical resistivity in oxidized vanadium films grown by the GLAD technique, Surf. Coat. Technol. 304 (2016) 476–485. doi:10.1016/j.surfcoat.2016.07.057.

[25] H. Zhang, Z. Wu, D. Yan, X. Xu, Y. Jiang, Tunable hysteresis in metal-insulator transition of nanostructured vanadium oxide thin films deposited by reactive direct current magnetron sputtering, Thin Solid Films. 552 (2014) 218–224. doi:10.1016/j.tsf.2013.12.007.

[26] G. Rampelberg, B. De Schutter, W. Devulder, K. Martens, I. Radu, C. Detavernier, In situ X-ray diffraction study of the controlled oxidation and reduction in the V-O system for the synthesis of VO_2 and V_2O_3 thin films, J.

Mater. Chem. C. 3 (2015) 11357–11365. doi:10.1039/c5tc02553b.

[27] Y.X. Ji, G.A. Niklasson, C.G. Granqvist, M. Boman, Thermochromic VO_2 films by thermal oxidation of vanadium in SO_2, Sol. Energy Mater. Sol. Cells. 144 (2016) 713–716. doi:10.1016/j.solmat.2015.10.012.

[28] P. Pedrosa, N. Martin, R. Salut, M. Arab Pour Yazdi, A. Billard, Controlled thermal oxidation of nanostructured vanadium thin films, Mater. Lett. 174 (2016) 162–166. doi:10.1016/j.matlet.2016.03.097.

[29] Q. Yu, W. Li, J. Liang, Z. Duan, Z. Hu, J. Liu, H. Chen, J. Chu, Oxygen pressure manipulations on the metal-insulator transition characteristics of highly (0 1 1)-oriented vanadium dioxide films grown by magnetron sputtering, J. Phys. D. Appl. Phys. 46 (2013) 055310. doi:10.1088/0022-3727/46/5/055310.

[30] H.M.R. Giannetta, C. Calaza, C. Calaza, L. Fonseca, L. Fraigi, L. Fonseca, Vanadium oxide thin films obtained by thermal annealing of layers deposited by RF magnetron sputtering at room temperature, in Modern technologies for creating the thin-film systems and coatings, by N. Nikitenkov, InTechOpen, London (2017). doi.org/10.5772/67054.

[31] J. Liang, X. Yu, Y. Zhao, X. Fan, W. Wu, S. Wang, Enhancement of metal-insulator transition performance of VO_2 thin films by conventional furnace annealing, Thin Solid Films. 730 (2021) 138709. doi:10.1016/j.tsf.2021.138709.

[32] M.H. Lee, Y. Kalcheim, J. Del Valle, I.K. Schuller, Controlling metal-insulator transitions in vanadium oxide thin films by modifying oxygen stoichiometry, ACS Appl. Mater. Interfaces. 13 (2021) 887–896. doi:10.1021/acsami.0c18327.

[33] A. Sohn, T. Kanki, K. Sakai, H. Tanaka, D.W. Kim, Fractal nature of metallic and insulating domain configurations in a VO_2 thin film revealed by Kelvin

probe force microscopy, Sci. Rep. 5 (2015) 10417. doi:10.1038/srep10417.

[34] N. Martin, A.R. Bally, P. Hones, R. Sanjinès, F. Lévy, High rate and process control of reactive sputtering by reactive gas pulsing: The Ti - O system, Thin Solid Films, 377–378 (2000) 550–556. doi:10.1016/S0040-6090(00)01440-1.

[35] H. Le Dreo, O. Banakh, H. Keppner, P.A. Steinmann, D. Briand, N.F. de Rooij, Optical, electrical and mechanical properties of the tantalum oxynitride thin films deposited by pulsing reactive gas sputtering, Thin Solid Films 515 (2006) 952–956. doi:10.1016/j.tsf.2006.07.054.

[36] T. Kubart, T. Polcar, O. Kappertz, N. Parreira, T. Nyberg, S. Berg, A. Cavaleiro, Modelling of magnetron sputtering of tungsten oxide with reactive gas pulsing, Plasma Process. Polym. 4 (3007) S522–S526. doi:10.1002/ppap.200731301.

[37] X. Xu, M. Arab Pour Yazdi, R. Salut, J.M. Cote, A. Billard, N. Martin, Structure, composition and electronic properties of tungsten oxide thin film sputter deposited by the reactive gas pulsing process, Mater. Chem. Phys. 205 (2018) 391–400. doi:10.1016/j.matchemphys.2017.11.048.

[38] A.J. Santos, M. Escanciano, A. Suárez-Llorens, M.P. Yeste, F.M. Morales, A novel route for the easy production of thermochromic VO_2 nanoparticles, Chem. Eur. J. (in press).

[39] M.J. Nieuwenhuizen, H.B. Haanstra, Microfractography of thin films, Philips Tech. Rev. 27 (1966) 87–91.

[40] R.N. Tait, T. Smy, M.J. Brett, Modelling and characterization of columnar growth in evaporated films, Thin Solid Films. 226 (1993) 196–201. doi:10.1016/0040-6090(93)90378-3.

[41] J. Lintymer, J. Gavoille, N. Martin, J. Takadoum, Glancing angle deposition to

modify microstructure and properties of sputter deposited chromium thin films, Surf. Coat. Technol. 174–175 (2003) 316–323. doi:10.1016/S0257-8972(03)00413-4.

[42] M.M. Hawkeye, M.J. Brett, Glancing angle deposition: Fabrication, properties, and applications of micro- and nanostructured thin films, J. Vac. Sci. Technol. A Vacuum, Surfaces, Films. 25 (2007) 1317. doi:10.1116/1.2764082.

[43] A. Barranco, A. Borras, A.R. Gonzalez-Elipe, A. Palmero, Perspectives on oblique angle deposition of thin films: From fundamentals to devices, Prog. Mater. Sci. 76 (2016) 59–153. doi:10.1016/j.pmatsci.2015.06.003.

[44] J. Dervaux, P.A. Cornier, P. Moskovkin, O. Douheret, S. Konstantinidis, R. Lazzaroni, S. Lucas, R. Snyders, Synthesis of nanostructured Ti thin films by combining glancing angle deposition and magnetron sputtering: A joint experimental and modeling study, Thin Solid films 636 (2017) 644–657. doi:10.1016/j.tsf.2017.06.006.

[45] A. Besnard, N. Martin, L. Carpentier, B. Gallas, A theoretical model for the electrical properties of chromium thin films sputter deposited at oblique incidence, J. Phys. D: Appl. Phys. 44 (2011) 215301–8. doi:10.1088/0022-3727/44/21/215301.

[46] G. Abadias, E. Chason, J. Keckes, M. Sebastiani, G.B. Thompson, E. Barthel, G.L. Doll, C.E. Murray, C.H. Stoessel, L. Martinu, Review Article: Stress in thin films and coatings: Current status, challenges, and prospects, J. Vac. Sci. Technol. A Vacuum, Surfaces, Film. 36 (2018) 020801. doi:10.1116/1.5011790.

[47] P. Shvets, O. Dikaya, K. Maksimova, A. Goikhman, A review of Raman spectroscopy of vanadium oxides, J. Raman Spectrosc. 50 (2019) 1226–1244.

doi:10.1002/jrs.5616.

[48] Y. Li, S. Ji, Y. Gao, H. Luo, M. Kanehira, Core-shell VO_2 @TiO_2 nanorods that combine thermochromic and photocatalytic properties for application as energy-saving smart coatings, Sci. Rep. 3 (2013) 1370. doi:10.1038/srep01370.

[49] P. Vilanova-Martínez, J. Hernández-Velasco, A.R. Landa-Cánovas, F. Agulló-Rueda, Laser heating induced phase changes of VO_2 crystals in air monitored by Raman spectroscopy, J. Alloys Compd. 661 (2016) 122–125. doi:10.1016/j.jallcom.2015.11.174.

[50] D. Louloudakis, D. Vernardou, E. Spanakis, M. Suchea, G. Kenanakis, M. Pemble, K. Savvakis, N. Katsarakis, E. Koudoumas, G. Kiriakidis, Atmospheric pressure chemical vapor deposition of amorphous tungsten doped vanadium dioxide for smart window applications, Adv. Mater. Lett. 7 (2016) 192–196. doi:10.5185/amlett.2016.6024.

[51] M.M. Margoni, S. Mathuri, K. Ramamurthi, R.R. Babu, K. Sethuraman, Sprayed vanadium pentoxide thin films: Influence of substrate temperature and role of HNO_3 on the structural, optical, morphological and electrical properties, Appl. Surf. Sci. 418 (2017) 280–290. doi:10.1016/j.apsusc.2017.02.039.

[52] A. Baltakesmez, C. Aykaç, B. Güzeldir, Phase transition and changing properties of nanostructured V_2O_5 thin films deposited by spray pyrolysis technique, as a function of tungsten dopant, Appl. Phys. A Mater. Sci. Process. 125 (2019) 1–18. doi:10.1007/s00339-019-2736-0.

[53] C.O.F. Ba, S.T. Bah, M. D'Auteuil, V. Fortin, P. V. Ashrit, R. Vallée, VO_2 thin films based active and passive thermochromic devices for energy management applications, Curr. Appl. Phys. 14 (2014) 1531–1537.

doi:10.1016/j.cap.2014.09.005.

[54] L. Kang, Y. Gao, Z. Zhang, J. Du, C. Cao, Z. Chen, H. Luo, Effects of annealing parameters on optical properties of thermochromic VO_2 films prepared in aqueous solution, J. Phys. Chem. C. 114 (2010) 1901–1911. doi.org/10.1021/jp909009w.

[55] T.G. Sparrow, B.G. Williams, C.N.R. Rao, J.M. Thomas, L_3/L_2 white-line intensity ratios in the electron energy-loss spectra of 3d transition-metal oxides, Chem. Phys. Lett. 108 (1984) 547–550. doi:10.1016/0009-2614(84)85051-4.

[56] O.L. Krivanek, J.H. Paterson, Elnes of 3d transition-metal oxides. I. Variations across the periodic table, Ultramicroscopy. 32 (1990) 313–318. doi:10.1016/0304-3991(90)90077-Y.

[57] W.G. Waddington, P. Rez, I.P. Grant, C.J. Humphreys, White lines in the $L_{2,3}$ electron-energy-loss and x-ray absorption spectra of 3d transition metals, Phys. Rev. B. 34 (1986) 1467–1473. doi:10.1103/PhysRevB.34.1467.

[58] A. Gloter, V. Serin, C. Turquat, C. Cesari, C. Leroux, G. Nihoul, Vanadium valency and hybridization in V-doped hafnia investigated by electron energy loss spectroscopy, Eur. Phys. J. B. 22 (2001) 179–186. doi:10.1007/PL00011142.

[59] D.S. Su, M. Wieske, E. Beckmann, A. Blume, G. Mestl, R. Schlögl, Electron beam induced reduction of V_2O_5 studied by analytical electron microscopy, Catal. Lett. 75 (2001) 81–86. doi:10.1023/A:1016754922933.

[60] X.W. Lin, Y.Y. Wang, V.P. Dravid, P.M. Michalakos, M.C. Kung, Valence states and hybridization in vanadium oxide systems investigated by transmission electron-energy-loss spectroscopy, Phys. Rev. B - Condens. Matter. 47 (1993) 3477. doi:10.1126/science.267.5198.713.

[61] C. Hébert, M. Willinger, D.S. Su, P. Pongratz, P. Schattschneider, R. Schlögl, Oxygen K-edge in vanadium oxides: Simulations and experiments, Eur. Phys. J. B. 28 (2002) 407–414. doi:10.1140/epjb/e2002-00244-4.

[62] J. Li, B.D. Gauntt, J. Kulik, E.C. Dickey, Stoichiometry of nanocrystalline VO_x thin films determined by electron energy loss spectroscopy, Microsc. Microanal. 15 (2009) 1004–1005. doi:10.1017/S1431927609092770.

[63] A.J. Santos, B. Lacroix, F. Maudet, A. Corvisier, F. Paumier, C. Dupeyrat, T. Girardeau, R. García, F.M. Morales, Surface oxidation of amorphous Si and Ge slanted columnar and mesoporous thin films: Evidence, scrutiny and limitations for infrared optics, Appl. Surf. Sci. 493 (2019) 807-817. doi:10.1016/j.apsusc.2019.07.064.

[64] M. Abbate, H. Pen, M.T. Czyzyk, F.M.F. de Groot, J.C. Fuggle, Y.J. Ma, C.T. Chen, F. Sette, A. Fujimori, Y. Ueda, K. Kosuge, Soft X-ray absorption spectroscopy of vanadium oxides, J. Electron Spectros. Relat. Phenomena. 62 (1993) 185–195. doi:10.1016/0368-2048(93)80014-D.

[65] C. Ko, Z. Yang, S. Ramanathan, Work function of vanadium dioxide thin films across the metal-insulator transition and the role of surface nonstoichiometry, ACS Appl. Mater. Interfaces. 3 (2011) 3396–3401. doi:10.1021/am2006299.

[66] S. Yu, S. Wang, M. Lu, L. Zuo, A metal-insulator transition study of VO_2 thin films grown on sapphire substrates, J. Appl. Phys. 122 (2017) 235102. doi:10.1063/1.4997437.

[67] A. Gupta, R. Aggarwal, P. Gupta, T. Dutta, R.J. Narayan, J. Narayan, Semiconductor to metal transition characteristics of VO_2 thin films grown epitaxially on Si (001), Appl. Phys. Lett. 95 (2009) 111915.

doi:10.1063/1.3232241.

[68] L. Chen, X. Wang, D. Wan, Y. Cui, B. Liu, S. Shi, H. Luo, Y. Gao, Tuning the phase transition temperature, electrical and optical properties of VO_2 by oxygen nonstoichiometry: Insights from first-principles calculations, RSC Adv. 6 (2016) 73070–73082. doi:10.1039/c6ra09449j.

[69] T.J. Huffman, D.J. Lahneman, S.L. Wang, T. Slusar, B.J. Kim, H.T. Kim, M.M. Qazilbash, Highly repeatable nanoscale phase coexistence in vanadium dioxide films, Phys. Rev. B. 97 (2018) 085146. doi:10.1103/PhysRevB.97.085146.

Figures and captions

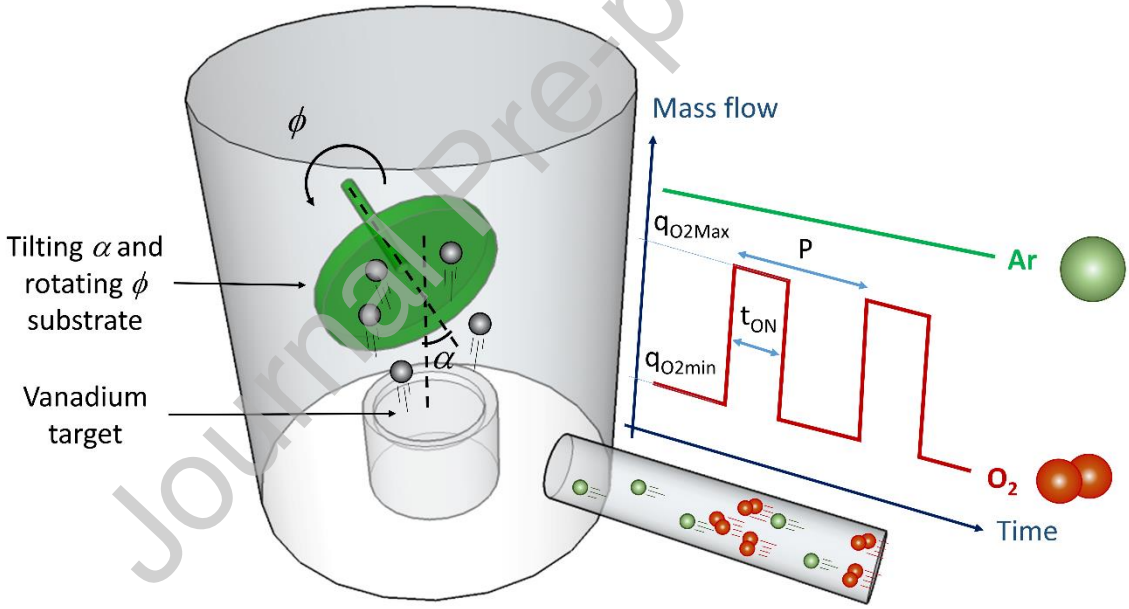

Fig. 1. Schematic view of the sputtering system used to deposit vanadium and vanadium oxide films combining GLancing Angle Deposition (GLAD) and Reactive Gas Pulsing Process (RGPP) techniques. The substrate can be inclined (α), fixed or rotated (ϕ) during the deposition. Oxygen gas is injected following rectangular pulses with a constant pulsing period P. The time of injection (t_{ON} time) is changed from 0 to 8 s.

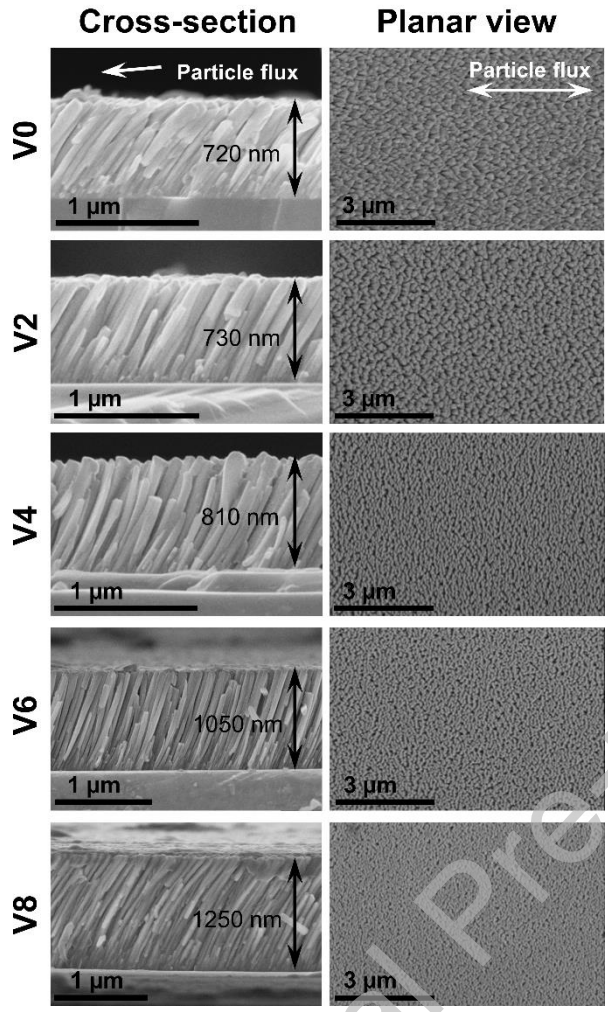

Fig. 2. SEM cross-section and planar view micrographs of the as-deposited vanadium or vanadium oxide GLAD films. The white arrows indicate the directions of the particle flux during GLAD deposition.

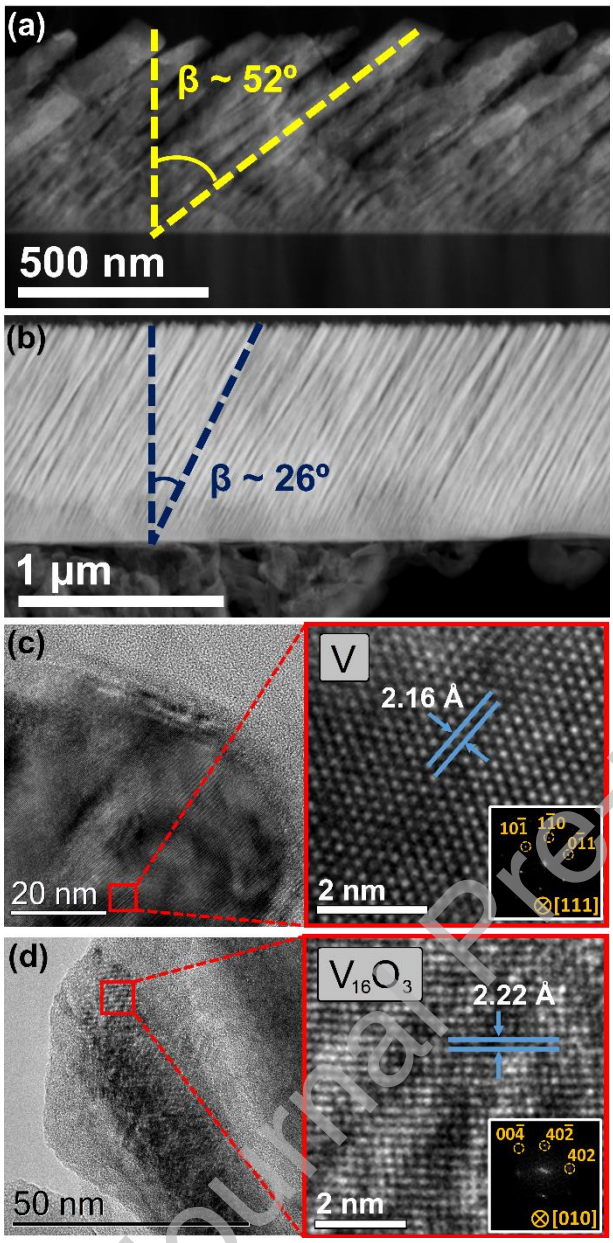

Fig. 3. TEM studies of the as-deposited V0 and V8 samples. Cross-section STEM-HAADF overviews of the (a) V0 and (b) V8 samples. High-resolution TEM micrographs of the (c) V0 and (d) V8 samples. The insets show magnified views of intragrain regions together with their corresponding FFT diffractions.

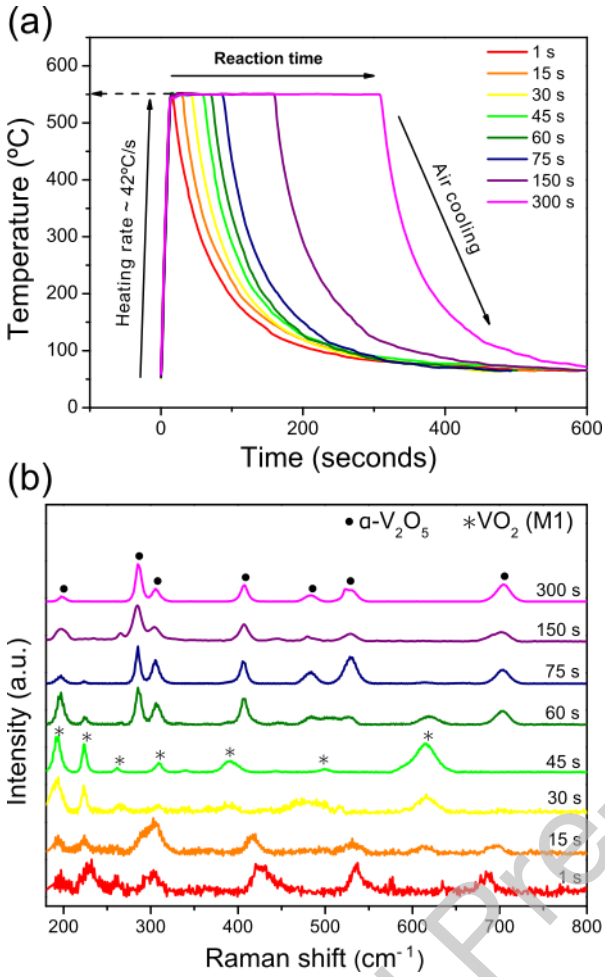

Fig. 4. (a) Temperature versus time tracks of many thermally treated V0 samples at 550ºC, h_r = 42ºC s^{-1}, and reaction times (t_r) ranging from 1 to 300 s. (b) Raman spectra of all the thermally treated V0 samples.

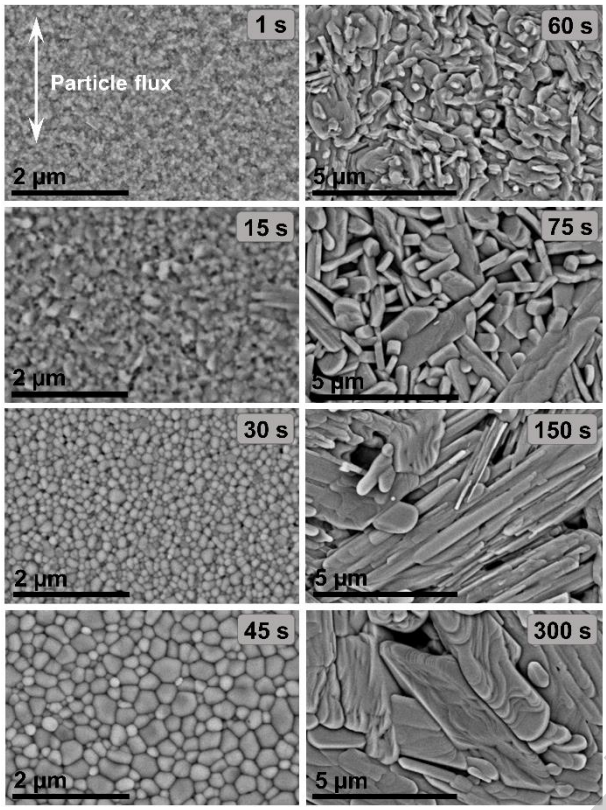

Fig. 5. SEM planar view of thermally treated V0 samples at 550ºC, h_r = 42ºC s^{-1}, and reaction times (t_r) ranging from 1 to 300 s as labelled in the images. The white arrow indicates the directions of the particle flux during GLAD deposition.

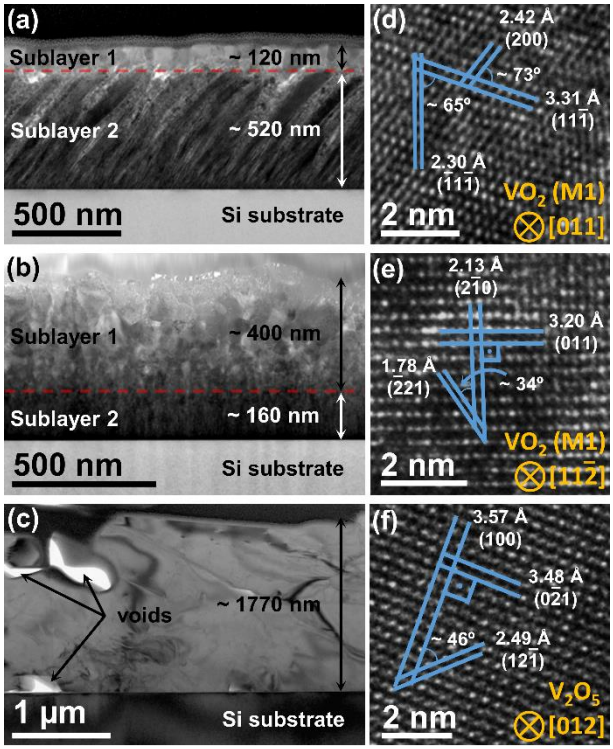

Fig. 6. TEM studies of thermally treated V0 samples. Bright-field (BF) TEM overview of V0 samples subjected to reaction times of (a) 1, (b) 45, and (c) 300 s. High-resolution TEM micrographs acquired from the upper regions of V0 samples subjected to reaction times of (d) 1 and (e) 45 s. (f) High-resolution TEM image of a representative region the of V0 sample subjected to a reaction time of 300 s.

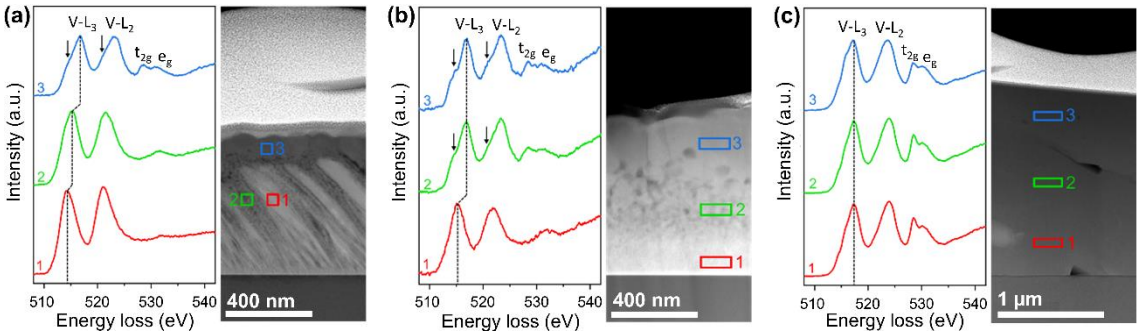

Fig. 7. EELS spectra recorded in different areas of thermally treated V0 samples at 550ºC, hr = 42ºC s^{-1}, and t_r = (a) 1 s, (b) 45 s, (c) 300 s. Images on the right corresponds to HAADF overviews. The spectra were previously aligned, and background-subtracted using a power law function.

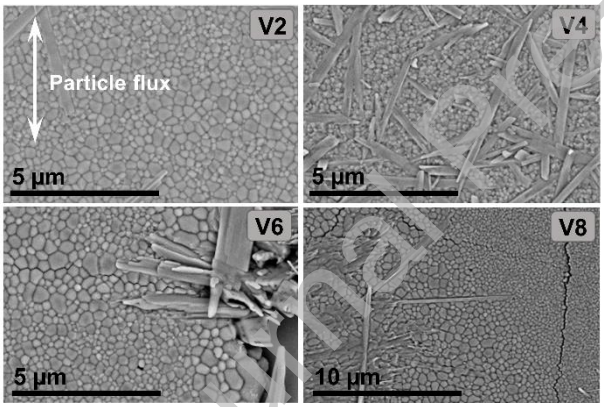

Fig. 8. SEM planar view of V2, V4, V6 and V8 samples after being thermally treated at 550ºC, h_r = 42ºC s^{-1} and t_r = 45 s.

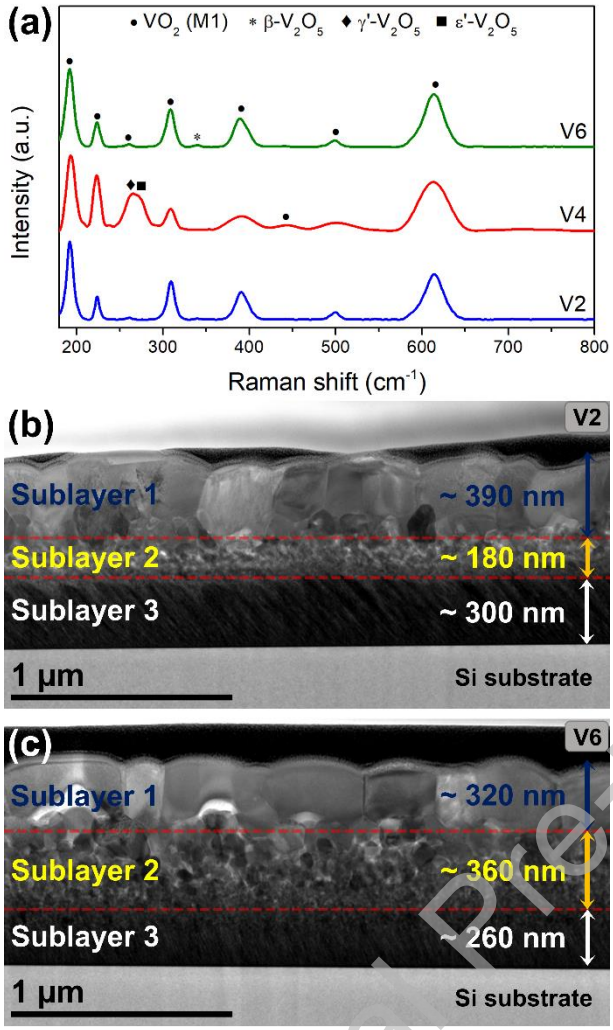

Fig. 9. (a) Raman spectra of V2, V4 and V6 samples after being thermally treated at 550ºC, h_r = 42ºC s^{-1} and t_r = 45 s. Bright-field (BF) TEM overview of (b) V2 and (c) V6 samples after being subjected to the abovementioned thermal treatment.

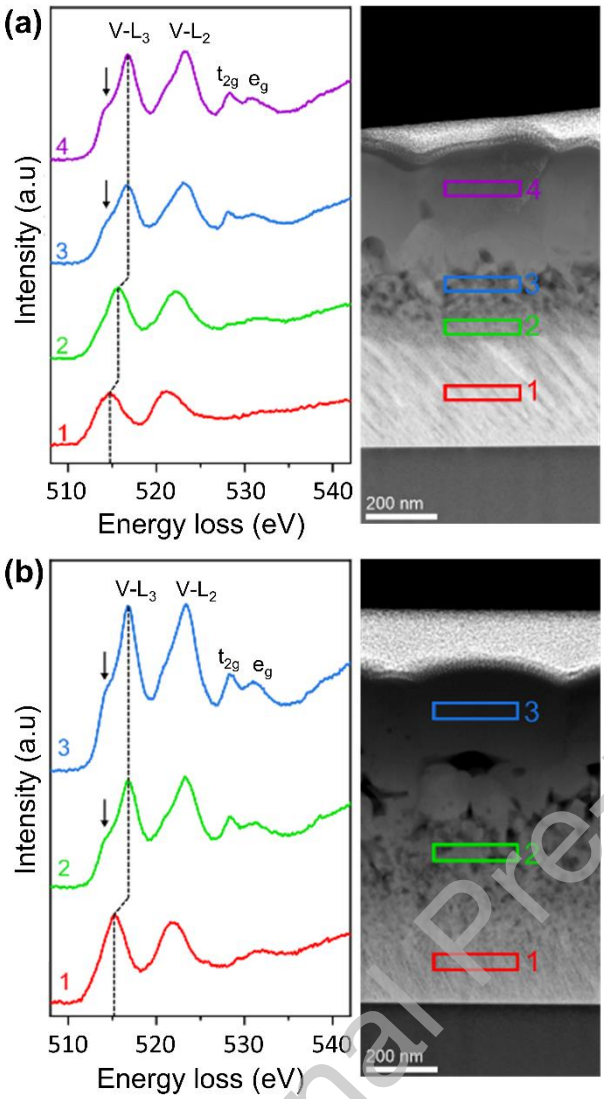

Fig. 10. EELS spectra recorded in different areas of V2 (a) and V6 (b) samples after thermal treatment at 550ºC, h_r = 42ºC s^{-1} and t_r = 45 s. Images on the right corresponds to HAADF overviews. The spectra were previously aligned, and background-subtracted using a power law function.

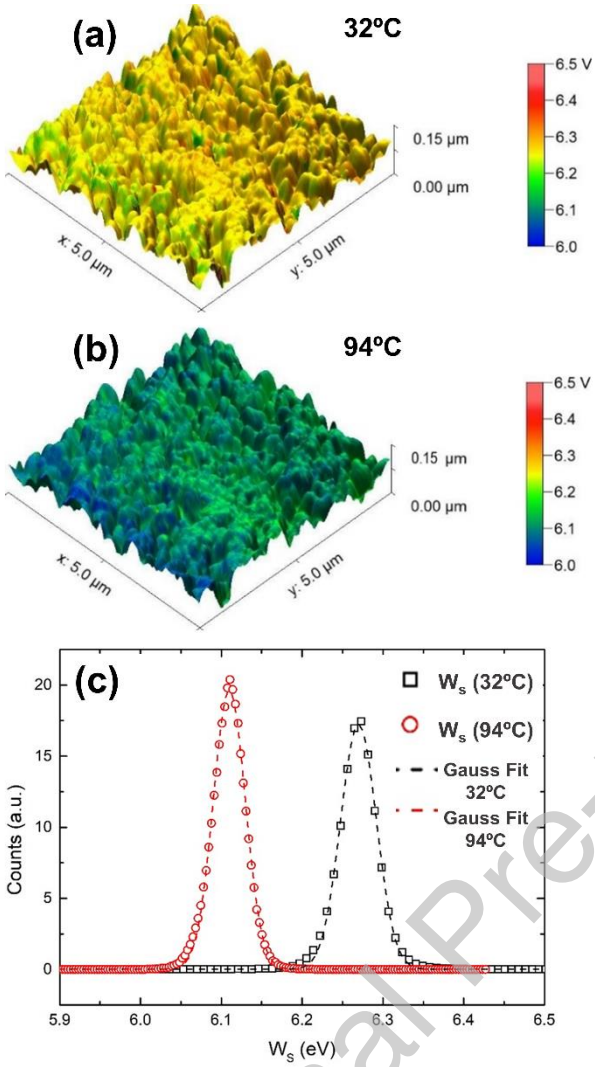

Fig. 11. Overlay of work function map and topography at two different temperatures, (a) below and (b) above MIT, for the V0 sample subjected to t_r = 45 s. (c) Distributions of work function values across these two maps; the mean (peak) values deduced from the Gauss fits are 6.27 eV at 32ºC and 6.11 eV at 94ºC, i.e., a value of ΔW_S = 0.16 eV for the MIT in this sample.

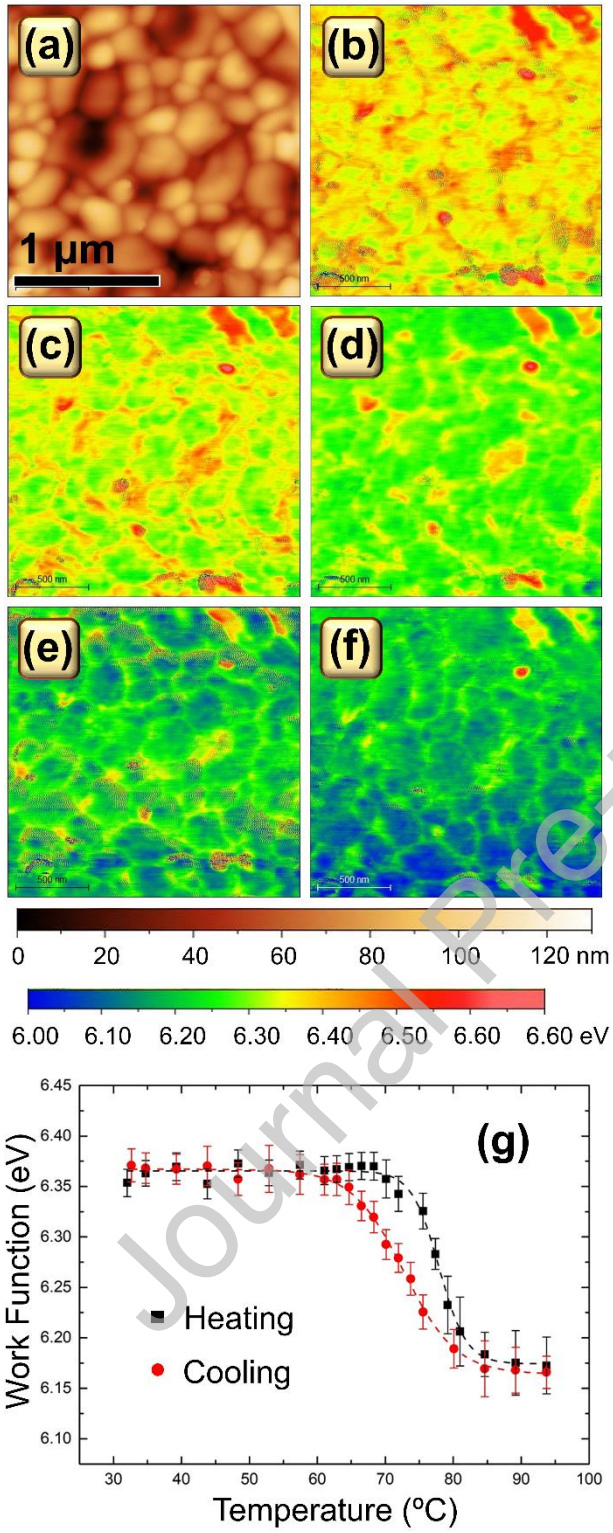

Fig. 12. Variable temperature KPFM measurements performed on the V2 sample after thermal treatment at 550ºC, h_r = 42ºC s^{-1} and t_r = 45 s. (a) AFM image of the region where the KPFM experiment was performed. (b) – (f) Work function maps for 70.1,

73.7, 77.4, 81.0 and 93.7°C, respectively, during heating. (g) Work function versus sample temperature during heating (black squares) and cooling (red circles) experiments performed on the V2 sample. These values are derived from the means of the Gaussian fits obtained from the distribution of surface potential values across the sample surface, considering the previously calibrated tip work function.

Tables and captions

Table 1. Operating conditions recorded during the sputter-deposition of vanadium and vanadium oxide films combining GLAD+RGPP.

Oxygen injection time t_{ON} (s)	0	2	4	6	8
Target potential (V)	312	311-321	307-314	305-312	309-324
Total sputtering pressure ($\times 10^{-3}$ mbar)	3.00	3.00-3.01	3.00-3.08	3.00-3.08	3.00-3.07
Deposition rate (nm h^{-1})	240	262	285	247	210

Table 2. Summary of the mean VO_2 grain sizes formed in the top sublayer for the different samples studied after being subjected to thermal treatments. Note that these values were extracted from the analysis of the different plan view SEM images collected.

Sample	**Average grain size (nm)**
V0 (t_r = 1 s)	88 ± 23
V0 (t_r = 15 s)	142 ± 60
V0 (t_r = 30 s)	173 ± 41
V0 (t_r = 45 s)	283 ± 116
V2	450 ± 129
V4	209 ± 57
V6	348 ± 164
V8	454 ± 185